



Variable Frequency Phase-Shift Modulation Symmetrical Series-Resonant Bidirectional DC-DC Converter-Analysis and Verification of ZVS Performance and Reactive Power Minimization-

Mishima, Tomokazu

Koga, Yasutaka

(Citation)

IEEJ Journal of Industry Applications, 10(5):540-553

(Issue Date)

2021-09-01

(Resource Type)

journal article

(Version)

Version of Record

(Rights)

© 2021 The Institute of Electrical Engineers of Japan

(URL)

<https://hdl.handle.net/20.500.14094/90009165>



Variable Frequency Phase-Shift Modulation Symmetrical Series-Resonant Bidirectional DC-DC Converter—Analysis and Verification of ZVS Performance and Reactive Power Minimization—

Tomokazu Mishima^{*a)} Senior Member, Yasutaka Koga^{*} Non-member

(Manuscript received Feb. 17, 2021, revised April 22, 2021)
J-STAGE Advance published date : May 28, 2021

Conventional dual active bridge (DAB) converters based on the non-resonant circuit topology have the severe limitation of soft switching under light load conditions without complex multi-pulse modulations such as dual or triple phase shift. To address this technical problem, this paper explores a symmetrical series-resonant bidirectional dc-dc converter (SSR-BDC). The SSR-BDC features the variable frequency phase shift modulation (VF-PSM) for the minimization of reactive power in a wide range of soft switching operations. The *CLLC* series resonant tanks provide symmetrical steady-state characteristics of the load power and voltage regulations in forward and reverse power flows, which is advantageous for the seamless exchange of power flows in power electronics applications based on a simple control logic. The principle of the power regulation is described with the frequency-domain analysis of SSR-BDC, whereby the theory for determining the most suitable phase shift angle is clarified. The experimental verifications on a 500 W prototype are presented, and the practical effectiveness is revealed; the actual efficiency improves by 1.4% and reactive power reduces by 75% after adopting the VF-PSM.

Keywords: phase shift (PS) modulation, series resonant bidirectional dc-dc converter, reactive power reduction, variable frequency, zero voltage soft switching (ZVS)

1. Introduction

High frequency (HF)-link bidirectional dc-dc converter (BDC) provides a continuous power flow with galvanic isolation between two dc voltage sources in the wide variety of power supplies such as solid-state transformer (SST) in renewable and sustainable energy generation, transportation and automotive power units, and uninterruptible power supply. The power converter architecture of typical SST is illustrated in Fig. 1. The dual active bridge (DAB) is the most popular technology as a BDC, and tremendous amounts of literatures have been published during the past decades^{(1)–(7)}.

The non-resonant DAB converter is based on the phase shift modulation (PSM) between the two ac voltage sources linked with the inductive reactance. Fig. 2 illustrates the circuit topology and phase shift modulations in the DAB converter. The technical issues of DAB converter exist in the trade-off relationship between the extension of soft switching range and reduction of reactive power^{(8)–(10)}. Therefore, the switching frequency is limited within the several ten kilohertz, and the large dc-link capacitors are requested both at the primary and secondary-side power stages, which may be the serious obstacles for achieving high power density. The phase shift and pulse width modulation, dual phase shift

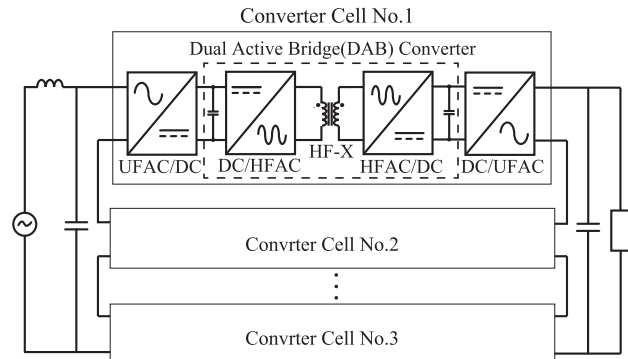


Fig. 1. Single-phase solid state transformer (SST) architecture based on BDCs.

(DPS)⁽¹¹⁾, and triple phase shift (TPS) strategies have been proposed for extension of soft switching range and reduction of reactive power in the DAB converters^{(12)–(13)}. However, the multi phase shift modulation (M-PSM) induces complexity in the controller design, whereby increment of the switching frequency is limited; the feasibility is still unclear at the present stage of development^{(13)–(14)}. In addition, the circulating currents inevitably emerge in the primary- and secondary-side full bridge circuits due to DPS or TPS schemes, consequently the power losses increase especially for the heavy voltage unbalance between the two dc voltages⁽¹⁵⁾. The M-PSM may induce the magnetic flux saturation of the high frequency transformer (HF-X) due to the unbalance phase shift angles.

In contrast to the conventional DAB converters, the

a) Correspondence to: Tomokazu Mishima. E-mail: mishima@maritime.kobe-u.ac.jp

^{*} Department of Oceanology, Marine Technology and Engineering Div, Faculty of Oceanology, Kobe University
5-1-1, Fukaeminami-machi, Higashinada-ku, Kobe, Hyogo 658-0022, Japan

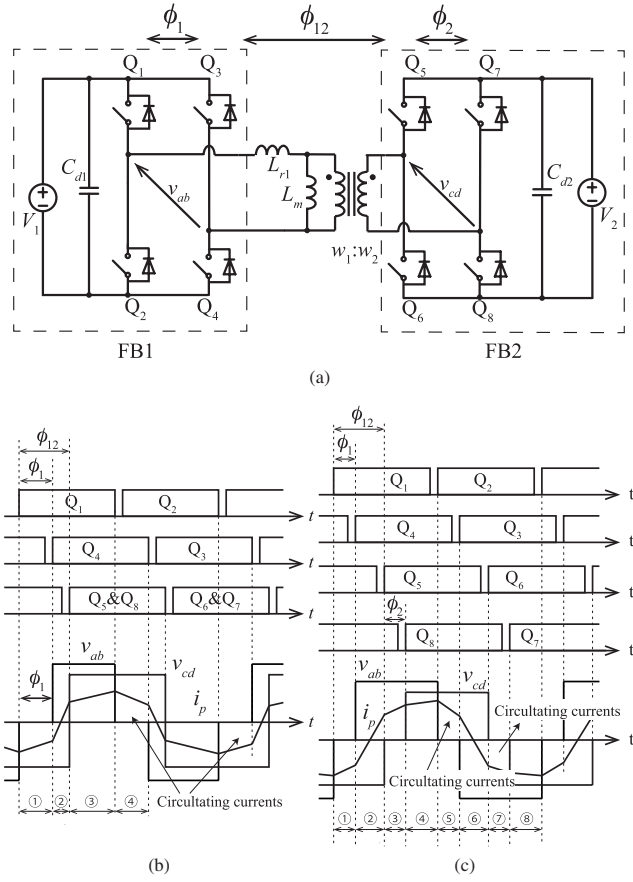


Fig. 2. Conventional DAB converter: (a) main circuit, (b) dual phase shift (DPS), and (c) triple phase shift (TPS) methodologies.

resonant bidirectional converter has attractive features such as a naturally soft commutation of power devices; therefore, a wide range of soft switching can achieve without any auxiliary circuits for expanding the soft switching range. The series resonant/series-parallel resonant converters (SRCs/SPRCs) have remarkable features such as a wide range of soft switching with the pulse frequency modulation (PFM). The resonant converter technology can also be effective for BDCs, and several RBDCs have been proposed for emerging power electronics applications such as wireless power transfer and battery charges for electric vehicles⁽¹⁶⁾⁻⁽¹⁷⁾.

Almost of the existing RBDCs are comprised of the asymmetrical resonant tanks, e.g. *LLC*, *LCLL* in the primary or secondary side of HF-X. The asymmetrical series resonant (ASR) BDCs are based on the principle of the inverter/rectifier combination. Accordingly, the steady-state characteristics of the dc voltage conversion ratio unequal between the forward and reverse power flows⁽¹⁸⁾⁻⁽²⁰⁾ since the magnetizing current of HF-X is not negligible. In addition, the seamless mode change of power flow cannot attain in the inverter/rectifier combination since power control is not available in the secondary-side rectifier. Thus, auxiliary passive components are required for achieving a wide range of soft switching with a seamless exchange of power flows⁽²¹⁾, which leads to the further complexity of the circuit configuration. Moreover, the bidirectional *LLC* converters suffer from parasitic ringing due to discontinuous current mode, which

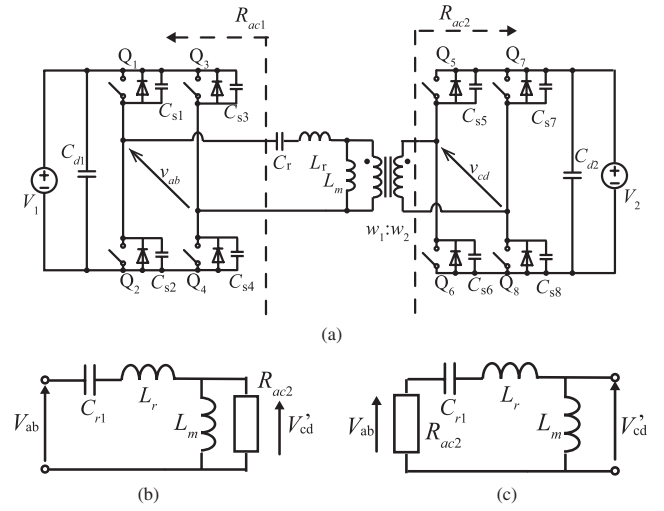


Fig. 3. Asymmetrical series resonant *LLC* BDC topology: (a) main circuit, (b) simplified equivalent circuit for the forward power flow and (c) for the reverse power flow.

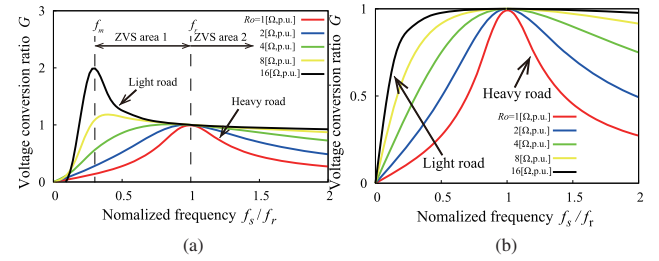


Fig. 4. Steady-state characteristics on voltage ratios of the symmetrical RBDC: (a) forward power flow, and (b) reverse power flow.

may raise an issue of radiation noises^{(4),(18)}. The ASR-BDCs depend on the magnetizing current and dead time tuning to achieve ZVS over the wide range of load power as well as the conventional DAB converters. Therefore, the power loss due to the high magnetizing current is outstanding in the light load region, and the dead time tuning is not effective any more once the magnetizing energy is smaller than the capacitive energy inside the full bridge circuit⁽²²⁾.

As a solution for the critical technical issues, the symmetrical series resonant (SSR) BDC is newly explored in this paper. The *CLLC* resonant tank-assisted SSR-BDCs have been proposed in the past literatures⁽²³⁾⁻⁽²⁷⁾. However, those converters are also based on the operating principle of inverter-rectifier combination for the forward and reverse power flows; it is not suitable for the seamless exchanges of the power flows. Analysis on the steady-state characteristics is carried out with the fundamental harmonics approximation (FHA). However, the circuit analysis based on a frequency domain only is not sufficient for the RBDC with PSM since the reactive power is not considered in this method. There are no past literatures dealing with the SSR-BDC on the soft switching range and reduction of reactive power with the combination of PSM and PFM, to the best of the authors' knowledge.

This paper presents the in-depth analysis and verifications of the SSR-BDC with variable frequency phase shift modulation (VF-PSM). The remarkable features of the RBDC

presented herein exist in a wide range of soft switching operation and effective reduction of reactive power without depending on the magnetizing current of HF transformer; Thus, high efficiency, small size filter and simple circuit configuration can be expected. The VF-PSM controlled BDCs have been reported in the past literatures^{(28)–(31)}, however the analysis and evaluations are limited on the conventional non-resonant DAB converters. The switching frequency varies over the wide range for the sake of non-resonant tanks. Accordingly, the design of the input and output filters are cumbersome, and the dynamics of power controller will be aggravated for the load variations.

The contribution of this paper is to demonstrate the profound comparison of pulse modulations based on PSM and PFM for SSR-BDC by the analytical and experimental verifications, which are the classical but most simple and practical power control scheme for the SSR-BDC. The rest of this paper is organized as follows: The circuit topology and mode-transitional operations are described in Section 2. The theory of VF-PSM is explained with the frequency-domain equivalent circuit of the SSR-BDC in Section 3, whereby the merit of VF-PSM is clarified in terms of reactive power reduction and wide range of soft switching. The power control scheme is introduced in Section 4, and the effectiveness is revealed by simulation in Section 5. The experimental results are demonstrated in Section 6 for evaluating the performance of the topology and control of SSR-BDC, after which the feasibility is summarized in Section 7.

2. Circuit Topology and Operations

The circuit topology of the SSR-BDC is depicted in Fig. 5⁽³²⁾. The series resonant tanks L_{r1} - C_{r1} and L_{r2} - C_{r2} contribute for producing the identical power transfer profiles in the forward and reverse power flows, which is useful for building a simple and practical controller. All the active switches Q_1 – Q_8 are commutated by ZVS with the aids of lossless snubber capacitors C_{s1} – C_{s8} , or a parasitic output capacitance of a unipolar semiconductor power device.

Fig. 6 illustrates the switching voltage and current waveforms with CF-PSM and VF-PSM. The lossless snubber capacitor is large enough for reducing the dv/dt rate at the turn-off transition for the heavy load with CF-PSM. The large snubber capacitor may result in the counter effect; The residual voltage emerges at the turn-off transitions under the condition of light load with CF-PSM, consequently the capacitive energy is discharged and ringing current appears at the turn-on transition. In contrast, the turn-off current can be reduced due to better power factor by VF-PSM. Introducing the series resonant tanks into the BDC is effective for minimizing a conduction current through the switches at their turn-on and turn-off transitions regardless of output power with the variable switching frequency. Therefore, ZVS can attain over the wide range of load power without increase of circulating currents, i.e. reactive powers both at the two dc voltage sources. Since the magnetizing inductance L_m of HF-X is much greater than the impedance of the series resonant tanks L_{r1} - C_{r1} and L_{r2} - C_{r2} , the magnetizing current i_m can be neglected while keeping ZVS in all the active switches. Accordingly, power loss due to the circulating current through L_m can be minimized as compared to *LLC* resonant converters.

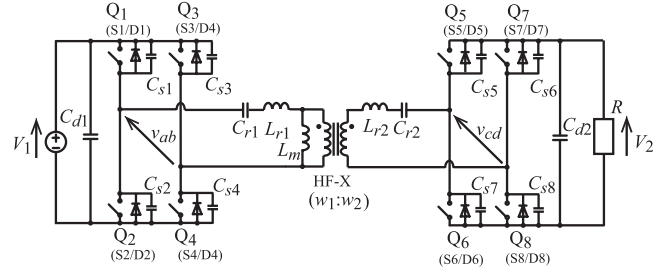


Fig. 5. Symmetrical series resonant *CLLC* bidirectional dc-dc converter with HF-link ($L_m \gg L_{rx}$, $x : 1, 2$).

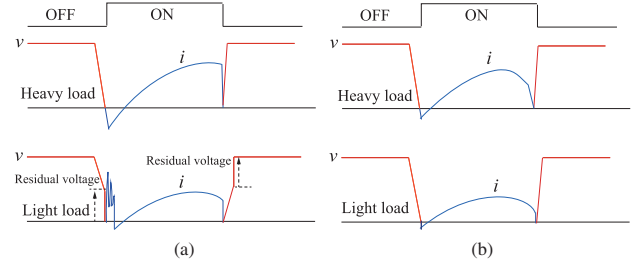


Fig. 6. Switch transitions of SSR-BDC: (a) CF-PSM and (b) VF-PSM.

In order to achieve ZVS in the active switches, the switching frequency f_s should be greater than the series resonant frequency f_r as

$$f_s > f_r = \frac{1}{2\pi \sqrt{(L_{r1} + L_{r2}') \frac{C_{r1}C_{r2}'}{C_{r1} + C_{r2}}}} \dots \dots \dots (1)$$

where $L_{r2}' = a^2 L_{r2}$ and $C_{r2}' = C_{r2}/a^2$ are the primary side-referred secondary-side parameters. The switching frequency f_s should be modulated around f_r in order to reduce the circulating current, i.e. reactive power.

Key operating waveforms and switching mode transitions are illustrated in Figs.7 and 8, respectively. The symbols δ^* represents the phase shift (PS) angle of signal stage between the leading and lagging-phase switches. On the other hand, the symbol δ denotes the PS angle of power stage between the bridge-leg voltages of the primary and secondary sides. Taking the dead time interval T_d into consideration, δ can be expressed in accordance with the voltage conditions as

$$\delta = \begin{cases} \delta^* - \delta_{T_d} & (\text{when } \hat{v}_{ab} > a\hat{v}_{cd}; \text{ buck mode}) \\ \delta^* + \delta_{T_d} & (\text{when } \hat{V}_{ab} < a\hat{V}_{cd}; \text{ boost mode}) \end{cases} \dots \dots \dots (2)$$

where δ_{T_d} corresponds to the phase angle of T_d and a ($= w_1/w_2$) represents the windings turns ratio of HF-X.

One switching cycle is divided into ten modes as follows:

- Mode 1 [power transfer mode in positive half cycle: $t \in [t_0, t_1]$] The polarity of the magnetizing current i_{Lm} reverses from negative to positive at $t = t_0$. Since the active switches Q_1 and Q_4 have already been on-state, active power starts to be fed from the input voltage source V_{in} to the load R_o . Accordingly, the primary-side current i_p of HF-R inverter gradually decays toward zero by the effect of series resonance.
- Mode 2 [Q_1 , Q_4 ZVS turn-off: $t \in [t_1, t_2]$] The gate signals for Q_1 and Q_4 are removed at $t = t_1$. Then, their

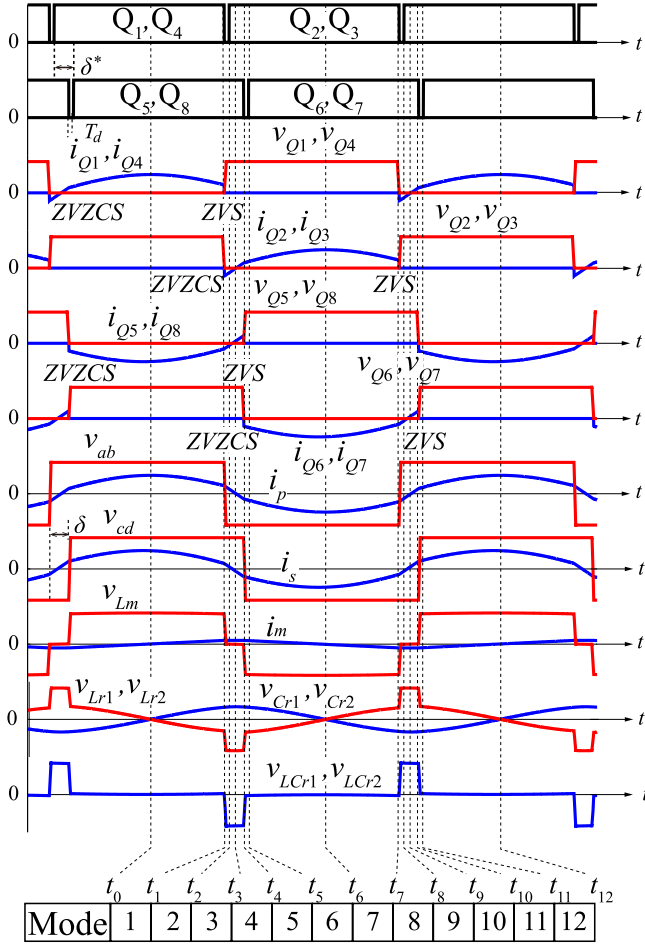


Fig. 7. Key operating voltage and current waveforms under the condition of forward power flow ($V_1 \rightarrow V_2$).

voltages v_{Q1} and v_{Q4} rise gradually from zero with the effects of parasitic, or the lossless snubber capacitors C_1 – C_4 , while the voltages v_{Q2} and v_{Q3} across Q_2 and Q_3 decrease gradually from V_{in} to zero. Thus, ZVS turn-off operations can perform in Q_1 and Q_4 . During this interval, ZVS condition can be expressed by

$$\frac{1}{2} L_{r1} i_p(t_1)^2 > 2 C_{s1} V_1^2 \dots \dots \dots (3)$$

$$i_p(t_1) > 0 \dots \dots \dots (4)$$

where the lossless snubber capacitors are identical as $C_{s1} = C_1 = C_2 = C_3 = C_4$. Accordingly, the minimum current $I_{p,min}$ of the primary-side HF-X for achieving ZVS is expressed by

$$I_{p,min} > \frac{2 V_1}{\zeta_1} \dots \dots \dots (5)$$

where $\zeta_1 (= \sqrt{L_{r1}/C_{s1}})$ denotes the resonant characteristics impedance of the primary-side series resonant tank.

- Mode 3 [Q_2, Q_3 ZVZCS turn-on: $t \in [t_2, t_3]$] The voltages v_{Q2} and v_{Q3} across Q_2 and Q_3 reach to zero at $t = t_2$ due to the edge-resonance sustaining from Mode 2, thereby D_2 and D_3 are forward-biased. During this interval, the gate terminals of Q_2 and Q_3 are triggered, and zero voltage and zero current soft switching (ZVZCS) turn-on commutation can be achieved in the two switches. At the same time i_p reverses its polarity, then i_s begins to rise gradually from zero.

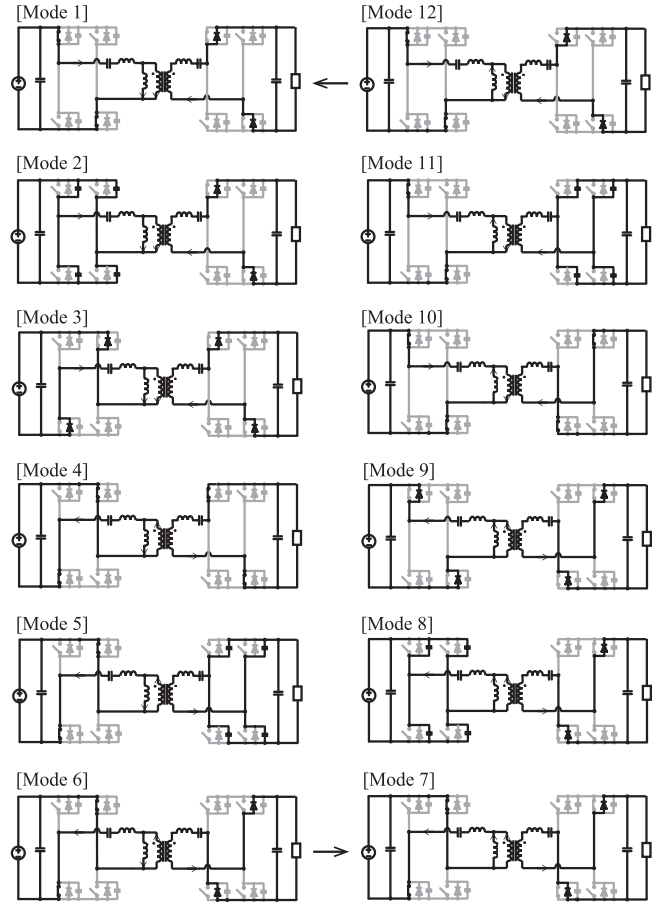


Fig. 8. Mode transitions and equivalent circuits during one switching cycle.

- Mode 4 [primary-side rectifier and secondary-side inverter mode: $t \in [t_3, t_4]$] The primary-side resonant current i_p reverses its polarity naturally at $t = t_3$ due to the series resonance. Accordingly, the primary-side switches Q_2 and Q_4 commute from D_2 and D_4 to S_2 and S_4 with minimization of reactive current, while the secondary-side switches Q_5 and Q_8 conduct in a forward direction similar to an inverter during the short interval.

- Mode 5 [Q_5, Q_8 ZVS turn-off mode: $t \in [t_4, t_5]$] The gate signals of Q_5 and Q_8 are removed at $t = t_4$, after which the voltages v_{Q5} and v_{Q8} rise linearly while v_{Q6} and v_{Q7} decay gradually toward to zero. Consequently, v_{Q5} and v_{Q8} are built up to V_{in} while v_{Q6} and v_{Q7} decrease to zero at the end of this interval. Thus, the ZVS turn-off transitions of Q_5 and Q_8 complete during this interval. The ZVS conditions for Q_5 and Q_8 are written as

$$\frac{1}{2} L_{r2} i_s(t_4)^2 > 2 C_{s2} V_2^2 \dots \dots \dots (6)$$

$$i_2(t_4) > 0 \dots \dots \dots (7)$$

where the lossless snubber capacitors are identical as $C_{s2} = C_5 = C_6 = C_7 = C_8$. Accordingly, the minimum current $I_{s,min}$ of the secondary-side full full-bridge inverter for achieving ZVS is expressed by

$$I_{s,min} > \frac{2 V_2}{\zeta_2} \dots \dots \dots (8)$$

where $\zeta_2 (= \sqrt{L_{r2}/C_{s2}})$ denotes the resonant characteristics impedance of the secondary-side series resonant

tank.

- Mode 6 [Q_6, Q_7 ZVZCS turn-on: $t \in [t_5, t_6]$] The gate terminals of secondary-side switches Q_6 and Q_7 are triggered at $t = t_5$ while their antiparallel diodes D_6 and D_7 are conducting. Accordingly, ZVZCS turn-on achieves simultaneously in Q_6 and Q_7 . Power transfer starts from V_{in} to the load in the negative half cycle.
- Mode 7 [power transfer mode in a negative half cycle: $t \in [t_6, t_7]$] The polarity of the magnetizing current i_m reverses from negative to positive at $t = t_6$. Since the active switches Q_2 and Q_3 are on-state, the power is fed from the input voltage source V_{in} to the load R_o and the negative half-cycle starts. The primary-side current i_p of HF-R inverter gradually decays toward zero by the effect of series resonance during this interval.
- Mode 8 [Q_2, Q_3 ZVS turn-off: $t \in [t_7, t_8]$] The gate signals for Q_2 and Q_3 are removed at $t = t_7$. Then, their voltages v_{Q2} and v_{Q3} rise gradually from zero with the effects of C_1 – C_4 , while the voltages v_{Q1} and v_{Q4} decrease gradually from V_{in} to zero. Thus, ZVS turn-off operation performs with i_p in Q_1 and Q_4 . During this interval, ZVS condition can be expressed by

$$\frac{1}{2} L_{r1} i_p(t_7)^2 > 2C_{s1} V_1^2 \dots\dots\dots (9)$$

$$i_p(t_7) > 0. \dots\dots\dots (10)$$

The minimum current $I_{p,min}$ of the primary-side HF-X for achieving ZVS is similarly expressed by (5).

- Mode 9 [Q_1, Q_4 ZVZCS turn-on: $t \in [t_8, t_9]$] The voltages v_{Q1} and v_{Q4} reach to zero at $t = t_8$ due to the edge-resonance sustaining from Mode 8, thereby D_1 and D_4 are forward-biased. During this interval, the gate terminals of Q_1 and Q_4 are triggered, thereby ZVZCS turn-on can attain in the two switches. At the same time, the polarity of i_p reverses and thereby i_s begins to rise gradually from zero.
- Mode 10 [primary-side rectifier and secondary-side inverter mode: $t \in [t_9, t_{10}]$] The primary-side resonant current i_p reverses its polarity naturally at $t = t_9$ due to the series resonance. Accordingly, the primary-side switches Q_1 and Q_4 commute from D_1 and D_4 to S_1 and S_4 with the minimization of reactive current, while the secondary-side switches Q_6 and Q_7 conduct in a forward direction similar to an inverter during the short interval.
- Mode 11 [Q_6, Q_7 ZVS turn-off mode: $t \in [t_{10}, t_{11}]$] The gate signals of Q_6 and Q_7 are removed at $t = t_{11}$, after which the voltages v_{Q6} and v_{Q7} rise linearly while v_{Q5} and v_{Q8} decay gradually toward to zero. Consequently, v_{Q5} and v_{Q8} are built up to V_{in} while v_{Q6} and v_{Q7} decrease to zero at the end of this interval. Thus, the transitions of Q_5 and Q_6 complete ZVS turn-off during this interval. The ZVS conditions for Q_6 and Q_7 are written as

$$\frac{1}{2} L_{r2} i_s(t_{11})^2 > 2C_{s2} V_2^2 \dots\dots\dots (11)$$

$$i_2(t_{11}) > 0. \dots\dots\dots (12)$$

The minimum current $I_{s,min}$ of the secondary-side full full-bridge inverter for achieving ZVS is similarly expressed by (8).

- Mode 12 [Q_5, Q_8 ZVZCS turn-on: $t \in [t_{11}, t_{12}]$] The gate terminals of secondary-side switches Q_5 and Q_8 are trig-

gered at $t = t_5$ while their antiparallel diodes D_5 and D_8 are conducting. Accordingly, ZVZCS turn-on achieves simultaneously in Q_5 and Q_8 . The power transfer starts from V_{in} to the load as the positive half cycle and return to the Mode 1.

The primary- and secondary-side full bridge circuits operate as the dual HF-R inverters with phase difference as explained above. The *CLLC* resonant tanks have no reluctance enough for storing inductive energy, therefore the most suitable operating point is the nominal voltage condition; $V_1 = aV_2$ named as “the unity voltage ratio”. For the area deviating from the unity voltage ratio, ZVS can maintain by extending the PS angle while the switching frequency changes in order to regulate output power. In the area with a large PS angle and switching frequency that exceeds over the limit of practical frequency variation, the single phase shift PWMs, i.e. primary-side PS-PWM (PPS) and secondary-side PS-PWM (SPS) techniques can be applied for the wide range of voltage regulations⁽³³⁾, although the significant amounts of circulating currents emerge similarly to DPS and TPS in Fig. 2.

3. Phasor Analysis of Symmetrical RBDC

3.1 Frequency Domain Analysis Sinusoidal ac analysis can be applied into the SSR-BDC in the steady state. The current waveforms of the HF-X are slightly distorted due to expansion of PS angle. However, the harmonics due to the PS angle are relatively small, accordingly the sinusoidal analysis can still keep effectiveness under the condition of the limited range of switching frequency variation just as similar to FHA in the *LLC* resonant converter⁽¹⁷⁾⁽³⁴⁾.

The simplified equivalent circuit of the SSR-BDC is indicated in Fig. 9. The two ac voltage sources \dot{V}_{ab} and $a\dot{V}_{cd}$ are defined with respect to their phase difference δ ($< \pi/2$) as

$$\dot{V}_{ab} = V_{ab} e^{j0} = V_{ab} = \frac{2\sqrt{2}V_1}{\pi} \dots\dots\dots (13)$$

$$\dot{V}_{cd} = V_{cd} e^{-j\delta} = \frac{2\sqrt{2}V_2}{\pi} e^{-j\delta} \dots\dots\dots (14)$$

The impedances of Fig. 9 are given by

$$\dot{Z}_1 = j(X_{L1} - X_{C1}) = (X_{L1} - X_{C1}) e^{j\frac{\pi}{2}} \dots\dots\dots (15)$$

$$\dot{Z}_2 = j(X_{L2} - X_{C2}) = (X_{L2} - X_{C2}) e^{j\frac{\pi}{2}} \dots\dots\dots (16)$$

$$\dot{Z}_m = jX_{Lm} = X_{Lm} e^{j\frac{\pi}{2}} \dots\dots\dots (17)$$

where the reactances of each reactive component are written with the angular frequency $\omega = 2\pi f_s$ as

$$X_{L1} = \omega L_{r1}, X_{L2} = \omega L_{r2}', X_{Lm} = \omega L_m \dots\dots\dots (18)$$

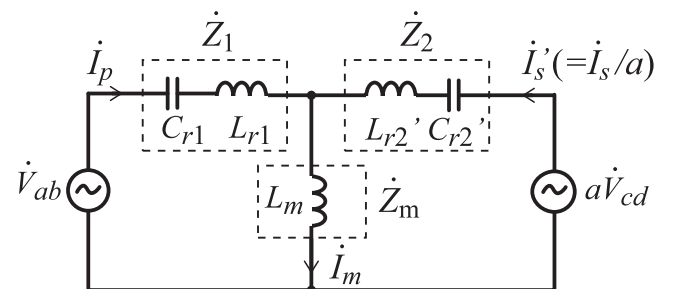


Fig. 9. Frequency-domain equivalent circuit of SSR-BDC.

$$i_p = \frac{(Z_m + Z_2)V_{ab} - aZ_m V_{cd} e^{-j\delta}}{Z_m(Z_1 + Z_2) + Z_1 Z_2} = \frac{aX_{Lm} V_{cd} \sin \delta}{\Gamma} - j \left\{ \frac{[X_{Lm} + (X_{L2} - X_{C2})]V_{ab} - aX_{Lm} V_{cd} \cos \delta}{\Gamma} \right\} \dots (20)$$

$$i_s' = \frac{(Z_m + Z_1)V_{cd} e^{-j\delta} - Z_m V_{ab}}{Z_m(Z_1 + Z_2) + Z_1 Z_2} = -\frac{\{X_{Lm} + (X_{L1} - X_{C1})\}aV_{cd} \sin \delta}{\Gamma} + j \left\{ \frac{X_{Lm} V_{ab} - [X_{Lm} + (X_{L1} - X_{C1})]aV_{cd} \cos \delta}{\Gamma} \right\} \dots (21)$$

$$i_m = \frac{Z_2 V_{ab} - Z_1 V_{cd} e^{-j\delta}}{Z_m(Z_1 + Z_2) + Z_1 Z_2} = -\frac{a(X_{L1} - X_{C1})V_{cd} \sin \delta}{\Gamma} - j \left\{ \frac{(X_{L2} - X_{C2})V_{ab} + a(X_{L1} - X_{C1})V_{cd} \cos \delta}{\Gamma} \right\} \dots (22)$$

$$\Gamma(\omega) = X_{Lm} \{(X_{L1} - X_{C1}) + (X_{L2} - X_{C2})\} + (X_{L1} - X_{C1})(X_{L2} - X_{C2}). \dots (23)$$

$$P_{e1} = \text{Re}(V_{ab} \bar{i}_p) = \frac{aX_{Lm} V_{ab} V_{cd} \sin \delta}{\Gamma} \simeq \frac{aV_{ab} V_{cd} \sin \delta}{Z_1 + Z_2} \dots (24)$$

$$P_{e2} = \text{Re}(aV_{cd} e^{-j\delta} \bar{i}_s') = -\frac{aX_{Lm} V_{ab} V_{cd} \sin \delta}{\Gamma} \simeq -\frac{aV_{ab} V_{cd} \sin \delta}{Z_1 + Z_2} \dots (25)$$

$$P_{r1} = \text{Im}(V_{ab} \bar{i}_p) = \frac{\{X_{Lm} + (X_{L2} - X_{C2})\} V_{ab}^2}{\Gamma} - \frac{aX_{Lm} V_{ab} V_{cd} \cos \delta}{\Gamma} \simeq \frac{V_{ab}(V_{ab} - aV_{cd} \cos \delta)}{Z_1 + Z_2} \dots (26)$$

$$P_{r2} = \text{Im}(aV_{cd} e^{-j\delta} \bar{i}_s') = \frac{\{X_{Lm} + (X_{L1} - X_{C1})\} a^2 V_{cd}^2}{\Gamma} - \frac{aX_{Lm} V_{ab} V_{cd} \cos \delta}{\Gamma} \simeq \frac{aV_{cd}(aV_{cd} - V_{ab} \cos \delta)}{Z_1 + Z_2} \dots (27)$$

$$X_{C1} = \frac{1}{\omega C_{r1}}, \quad X_{C2} = \frac{1}{\omega C_{r2'}} \dots (19)$$

Then, the primary-side current vector \vec{i}_p , secondary-side current vector $\vec{i}_s' (= \vec{i}_s/a)$ and magnetizing current vector \vec{i}_m can be expressed respectively by (20)–(23).

Fig. 10 comparatively displays the RMS currents between \vec{i}_p , \vec{i}_s' and \vec{i}_m with the PS angle and switching frequency based on (20)–(22). The magnetizing reactance \bar{Z}_m is considered as much greater than \bar{Z}_1 and \bar{Z}_2 due to the effects of the symmetrical resonant tanks as discussed in Subsection 3.1. Accordingly, \vec{i}_m are much smaller than the others, so the equivalent circuit can be simplified further by eliminating L_m in Fig. 9. By neglecting power losses in the RBDC, the active powers P_{e1} , P_{e2} and reactive powers P_{r1} , P_{r2} at the primary and secondary sides can be defined in (24)–(27). It can be known from those equations that the active and reactive powers can be controlled simultaneously by varying the PS angle and switching frequency.

3.2 Determination of Phase Shift Angle ZVS performances in the DPS and TPS controlled DAB converters are load-dependent together with the complicated process of PS angle calculations. On the other hand, ZVS constraint of the SSR-BDC with VF-PSM are independent of load power owing to the series resonant tanks that make the turn-off current to be minimized in all the switches. This is the essential difference between the conventional DAB and the SSR-BDC.

The voltages and currents of the symmetrical RBDC with CF-PSM are described by phasor diagrams in Fig. 11 assuming the forward power flow from V_1 to V_2 . Note here that the magnetizing current phasor \vec{i}_m is neglected due to existence of the secondary-side resonant tank, the impedance of which is expressed as $\bar{Z}_2 \ll \bar{Z}_m$. The primary-side current vector \vec{i}_p and secondary-side current vector \vec{i}_s' should be in-

ductive, i.e., lagging phase with respect to \vec{V}_{ab} and $a\vec{V}_{cd}$ for attaining ZVS in all the switches. Accordingly, the phase angle δ that grants ZVS in both the primary and secondary-side full bridge circuits can be expressed from Fig. 11(b) and (c) as:

- Buck mode: $V_{ab} \geq aV_{cd}$
 $V_{ab} \cos \delta < aV_{cd} \dots (28)$

$$\delta > \cos^{-1} \frac{aV_{cd}}{V_{ab}} = \cos^{-1} aG = \delta_{base} \dots (29)$$

- Boost mode: $V_{ab} < aV_{cd}$
 $V_{ab} > aV_{cd} \cos \delta \dots (30)$

$$\delta < \cos^{-1} \frac{V_{ab}}{aV_{cd}} = \cos^{-1} \frac{1}{aG} = \delta_{base} \dots (31)$$

where $G (= V_{ab}/V_{cd} = V_1/V_2)$ represents the voltage ratio, and δ_{base} is the base value of PS angle.

In Fig. 11(a) for the unity voltage ratio, the switching frequency reduces with VF-PSM, which results in the shrinks of PS angle δ and amplitude of the voltage vector \vec{V}_{X_L} ; the vector points $A-C-D$ move into $A'-C'-D'$. The voltage vector \vec{V}_{X_L} is defined as

$$\vec{V}_{X_L} = (Z_1 + Z_2)\vec{i}_p e^{j\frac{\pi}{2}} \dots (32)$$

Accordingly, the phase differences of voltage and current vectors change so that power factor approaches unity in the primary and secondary-side circuits respectively.

In the buck and boost modes where the voltage ratio deviates from unity, the switching frequency f_s rises due to VF-PSM so that the amplitude of \vec{V}_{X_L} changes with the fixed amplitude of \vec{i}_p . In Fig. 11(b) for the buck mode, the PS angle δ enlarges with VF-PSM, then \vec{V}_{X_L} is extended; the vector points $A-C-D$ move into $A'-C'-D'$. Accordingly, the current vector \vec{i}_s' moves into the lagging phase area with respect to the voltage vector $a\vec{V}_{cd}$ ($\vec{OD} \rightarrow \vec{OD'}$); then ZVS condition

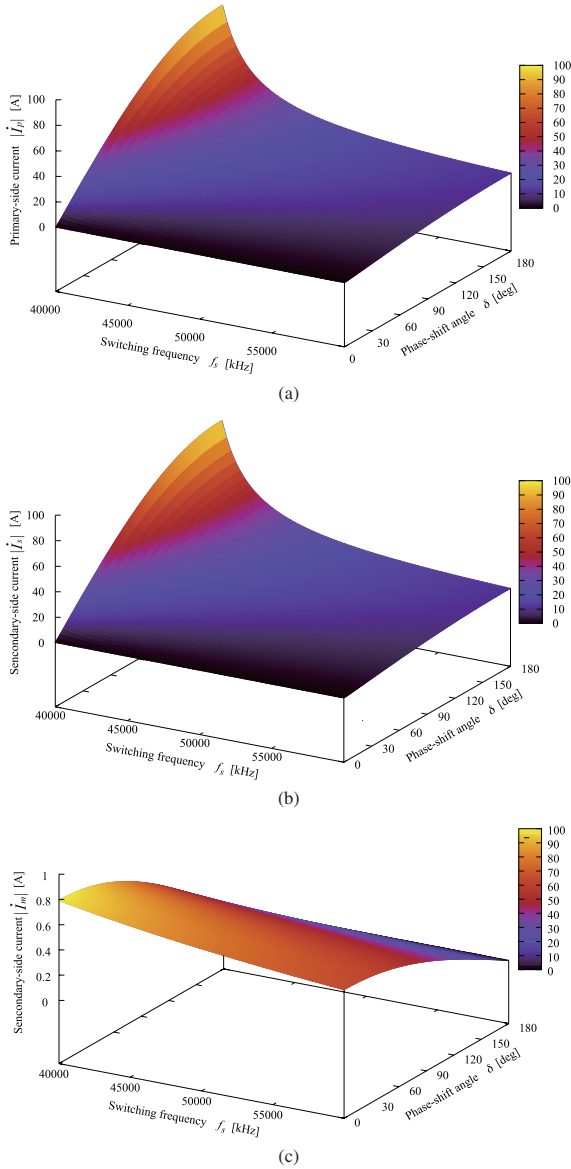


Fig. 10. RMS currents of i_p , i_s and i_m for the switching frequency and PS angle variations.

is satisfied in the secondary side as well as the primary side. In Fig. 11(c) for the boost mode, the PS angle δ enlarges in accordance with VF-PSM, then \dot{V}_{X_L} is extended; the vector points A - C - D shift into A' - C' - D' . Accordingly, the current vector \dot{I}_p moves into the lagging phase area with respect to the voltage vector \dot{V}_{ab} ($O\vec{A} \rightarrow O\vec{A}'$); then ZVS condition is satisfied in the primary side as well as the secondary side. It can be revealed from the phasor analysis that δ depends on the voltage conversion ratio G , not on the power command for ensuring ZVS in the VF-PSM scheme.

3.3 Power Factors The generalized phasor diagram in VF-PSM is revisited in Fig. 12. By using the cosine theorem herein, the power factor $\cos \theta_1$ of the primary side and $\cos \theta_2$ of the secondary side can be expressed respectively as

$$\cos \theta_1 = \cos\{\delta - (90^\circ - \lambda)\} \dots \dots \dots (33)$$

$$\cos \theta_2 = \cos(90^\circ + \lambda) \dots \dots \dots (34)$$

$$\lambda = \cos^{-1} \frac{aV_{cd} - V_{ab} \cos \delta}{\sqrt{V_{ab}^2 + (aV_{cd})^2 - 2aV_{cd}V_{ab} \cos \delta}} \dots \dots \dots (35)$$

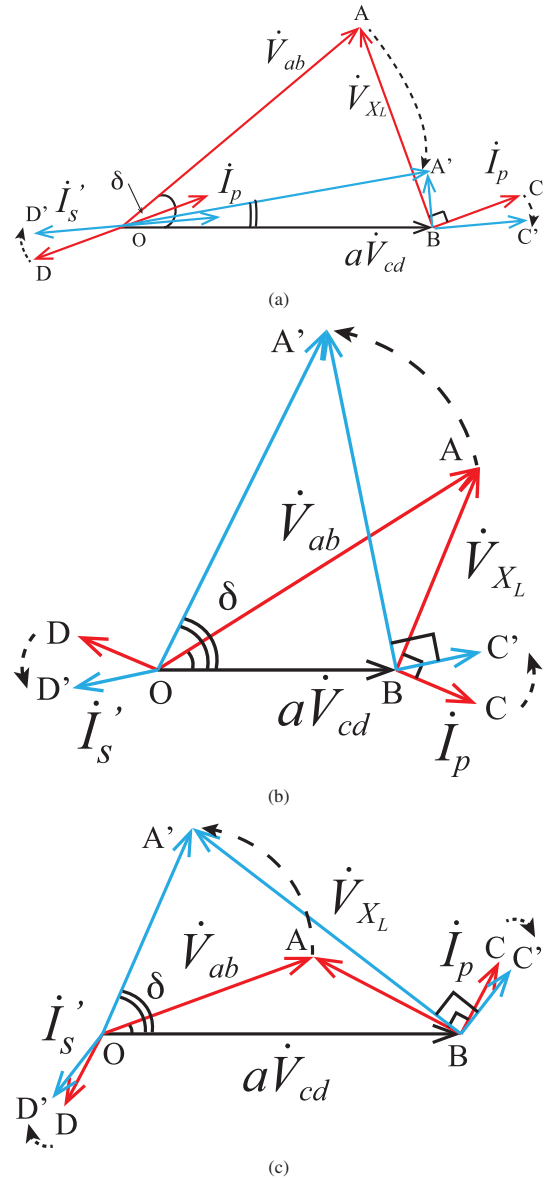


Fig. 11. Voltage and current phasors of CF-PSM (red arrows) and VF-PSM (blue arrows): (a) unity voltage ($V_{ab} = aV_{cd}$), (b) buck mode ($V_{ab} > aV_{cd}$), and (c) boost mode ($V_{ab} < aV_{cd}$).

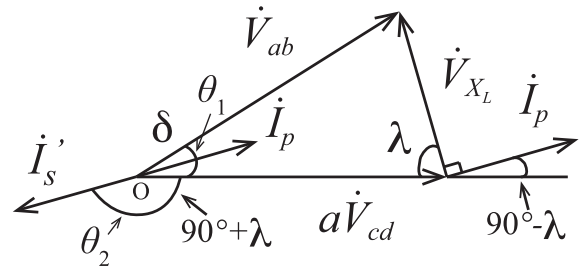


Fig. 12. Generalized phasor diagram with definition of power factors in VF-PSM.

Fig. 13 depicts the theoretical characteristics of power factor versus PS angle with respect to the voltage ratio, all of which are drawn from (33) and (34). The two power factors $\cos \theta_1$ and $\cos \theta_2$ are identical in the unity voltage ratio of $G = 1$ at any PS angle, and keep the high value as the PS angle reduces. In the buck mode of $G = 0.9$, $\cos \theta_1$ is lower than

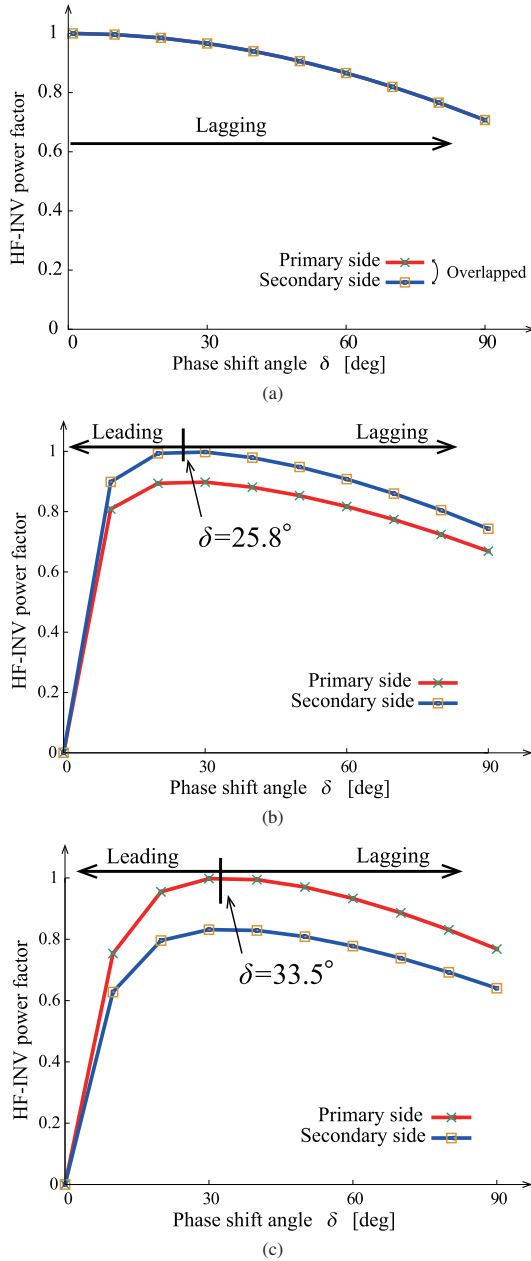


Fig. 13. Calculated power factors in the primary- and secondary-sides full bridge circuits on the basis of (33) and (34): (a) $G = 1$, (b) $G = 0.9$, and (c) $G = 1.2$.

$\cos \theta_2$, and the PS angle where the two power factors are maximum exists uniquely. In the boost mode of $G = 1.2$, $\cos \theta_2$ is lower than $\cos \theta_1$, and the PS angle where the two power factors are maximum exists uniquely. Thus, it can be revealed from Fig. 13 that power factors should be determined from the input and output dc voltage ratio in the SSR-BDC.

4. Power Control Scheme

Referring to the foregoing analyses, the output power P_o can be controlled by changing the switching frequency f_s once the PS angle δ is determined on the basis of the voltage conversion ratio G .

The schematic diagram of power controller for the SSR-BDC is presented in Fig. 14. The PS angle command δ^* consists of the base value δ_{base} and the additional angle δ_{add} .

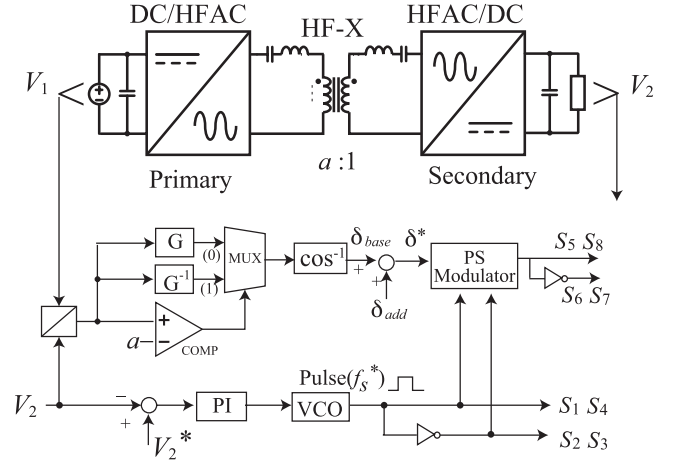


Fig. 14. Circuit diagram of the voltage mode controller.

According to the ZVS conditions of (29) and (31), δ_{base} is obtained from the voltage ratio G whereas δ_{add} is set so as to ensure lagging-phase currents for ZVS. It should be remarked here δ_{add} can be fixed owing to the minimized reactive power by switching frequency modulation.

$$t_{zvs} = C_{s1} \frac{V_1}{I_{p,min}} = a^2 C_{s2} \frac{V_2}{I_{s,min}} < T_d \dots \dots \dots (36)$$

where t_{zvs} denotes the transitional time for completing ZVS.

The additional PS angle δ_{add} in (2) can be determined from δ in $G = 1$, which is the minimum PS angle between \dot{V}_{ab} and $a\dot{V}_{cd}$.

5. Simulation Analysis

Performances of the SSR-BDC and control system are analyzed by simulation. The circuit parameters are as follows: $V_1 = 200$ V, $P_o = 2$ kW, $L_{r1} = L_{r2} = 40$ μ H, $C_{r1} = C_{r2} = 440$ μ H, resonant frequency $f_r = 40$ kHz, $a = 1$, and $\delta_{add} = 10^\circ$. The switching frequency f_s for CF-PSM is set as 45 kHz in order to attain ZVS at $G = 1$.

The steady-state characteristics on the load variations are depicted with the closed control loop in Fig. 15. The converter performance with CF-PSM experiences hard switching in the region out of $G = 1$. In contrast to that, the converter performance with VF-PSM keeps the soft switching under the wide range of voltage ratio ($G = 0.2$ – 2). It should be remarked here the larger the voltage unbalance is, the more outstanding the reactive powers emerges in the converter while ZVS can maintain.

The output power versus controlled valuables are compared in Figs. 16(a) and (b). In the case of CF-PSM, the operating points in one of the primary and secondary-side circuits are out of the soft switching except for $G = 1$. In contrast to that, ZVS can accomplish over the wide range of P_o by VF-PSM under the same condition of G .

The power factors of primary- and secondary-side inverters are illustrated in Figs. 17(a)–(c). In the unity voltage ratio $G = 1$, the power factors of the primary and secondary sides can stay over 0.99 by the effect of VF-PSM for the load variations while decline gradually according to increment of the load in CF-PSM. In the buck mode $G = 0.9$, the power factor of the primary side is a little lower than that of the secondary side in VF-PSM as discussed in Section 3.3, however ZVS

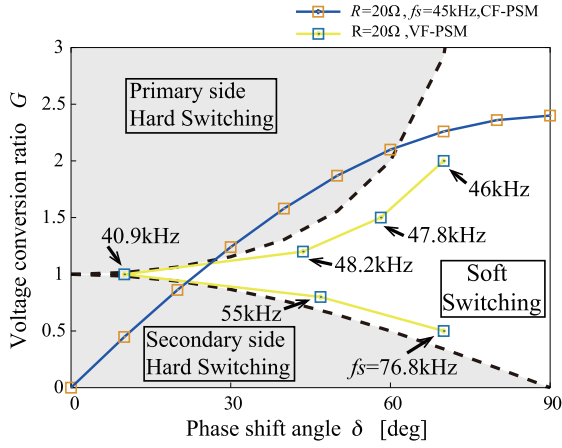


Fig. 15. Simulated steady-state curves of voltage conversion ratio versus phase shift angle with CF-PSM and VF-PSM schemes.

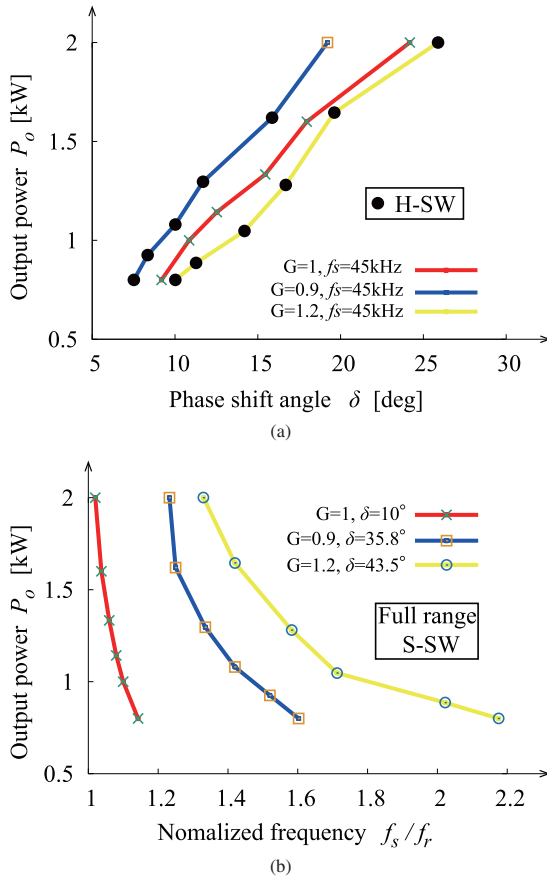


Fig. 16. Simulation results on output power control: (a) CF-PSM, and (b) VF-PSM.

can attain in the whole range of load variations at the both sides. On the other hand, the power factors decrease in the light load area by CF-PSM, and eventually the hard switching appears in the secondary side. In the boost mode $G = 1.2$, the power factor of the secondary side is a little lower than that of the primary side in VF-PSM, although ZVS can attain in the whole range of load variations as well as the buck mode. On the other hand, the power factors decrease in the light load area by CF-PSM, and then hard switching appears in the primary side. The comparative analysis herewith indicates VF-PSM are effective for maintaining the high efficiency from

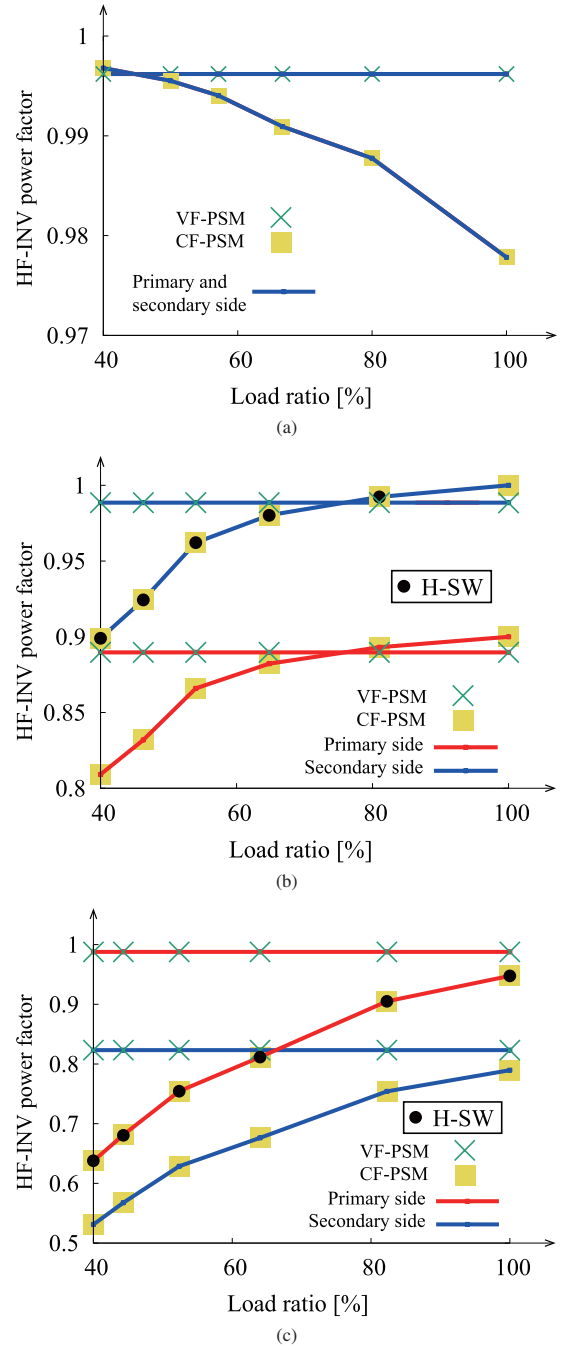


Fig. 17. Simulation results of power factors for load power variations: (a) $G = 1$, (b) $G = 0.9$, and (c) $G = 1.2$.

the viewpoints of soft switching range and power factors.

6. Experimental Results and Evaluation

The feasibility of the *CLLC* symmetrical RBDC is investigated by experiment of a 500 W prototype. The exterior appearance of the prototype is presented in Fig. 18, and its specification is summarized in Table 1. By referring to the simulation analysis mentioned above, the switching frequency for CF-PSM is fixed at 50 kHz in order to attain soft switching over the wide range of load variations.

6.1 Soft Switching Performances The observed cyclic waveforms of the RBDC with CF-PSM are depicted in Fig. 19. Although it is far from a typical behavior of hard

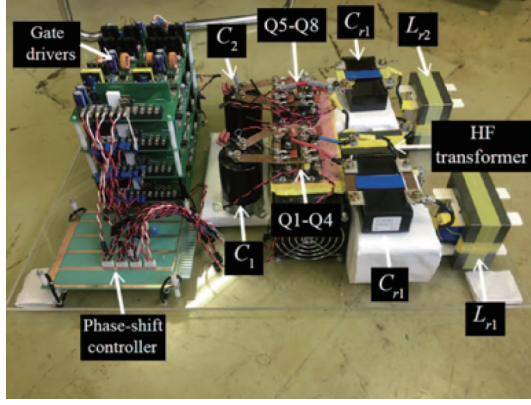
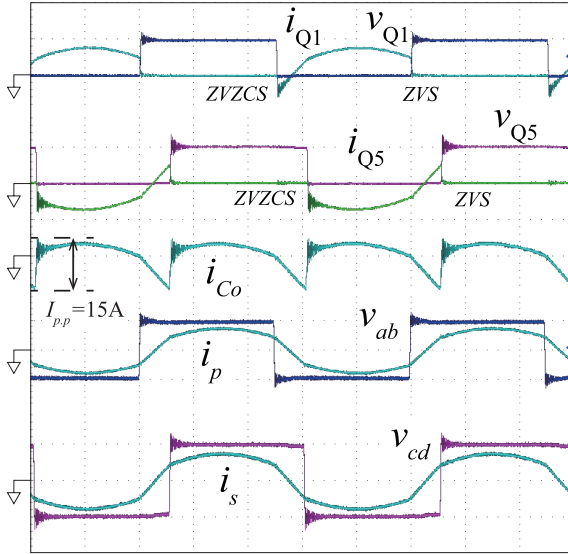


Fig. 18. Exterior appearance of the SSR-BDC prototype.

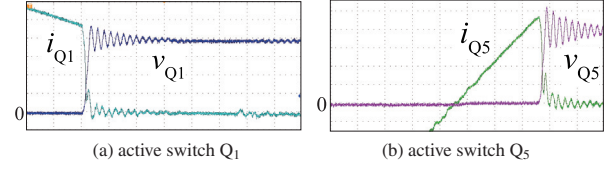
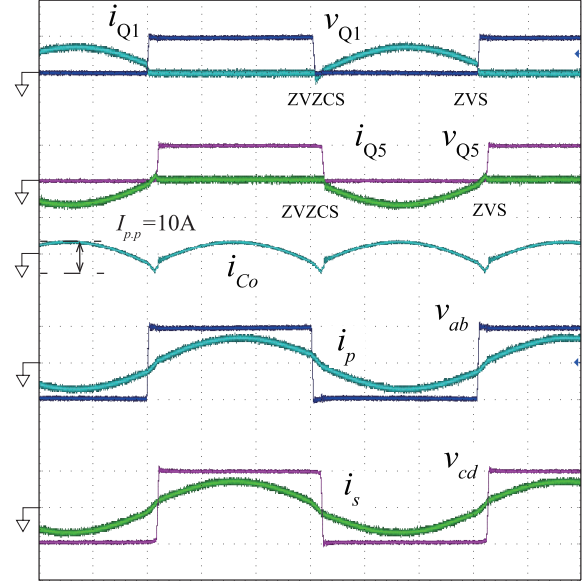
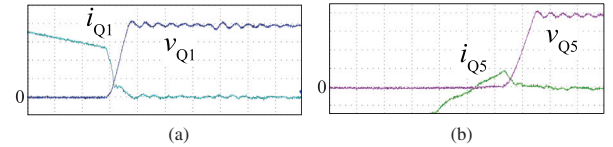
Table 1. Experimental Circuit Parameter and Conditions

Item	Symbol	Value [unit]
Nominal DC voltages	V_1, V_2	100[V]
Rated power	P_o	500[W]
Smoothing capacitors	C_{d1}, C_{d2}	1000[μF]
Series resonant capacitors	C_{r1}, C_{r2}	440[nF]
Series resonant inductors	L_{r1}, L_{r2}	40[μH]
HF-X magnetizing inductance	L_m	500[μH]
Snubbing capacitors in IGBTs	$C_{s1}-C_{s8}$	1[nF]
Resonant frequency	f_r	40[kHz]
Transformer turns ratio	a	1/1 ($= w_1/w_2$)

* $Q_1 - Q_8$: IGBT(IXGN60NC2D1, 600 [V], 75 [A])Fig. 19. Observed voltage and current waveforms of CF-PSM-based RBDC at $P_o = 500$ W, $f_s = 50$ kHz, and $\delta = 40^\circ$ (100 V/div, 10 A/div, and 4 μs/div): RSM currents $I_{Q1} = 3.0$ A, $I_{Q5} = 2.9$ A.

switching, a small amount of voltage surges and ripples appear at the turn-off transitions of Q_1 and Q_5 as clearly revealed in Fig. 20.

The observed cyclic waveforms of the RBDC with VF-PSM are depicted in Fig. 21. The peak-peak value $I_{p,p}$ of the displacement current i_{co} in C_o decreases from 15 A to 10 A; reduced by 35% as drawn in Figs. 19 and 21. The reactive powers are calculated as 178 Var with CF-PSM and 44 Var with VF-PSM, respectively. Thus, the reactive power reduces

Fig. 20. Enlarged waveforms of CF-PSM controlled SSR-BDC at $P_o = 500$ W, $f_s = 50$ kHz and $\delta = 40^\circ$ (25 V/div, 1 A/div, 400 ns/div).Fig. 21. Observed voltage and current waveforms of VF-PSM controlled SSR-BDC at $P_o = 500$ W, $f_s = 41$ kHz, and $\delta = 10^\circ$ (100 V/div, 10 A/div, and 4 μs/div): RSM currents $I_{Q1} = 2.7$ A, $I_{Q5} = 2.5$ A.Fig. 22. Enlarged waveforms of VF-PSM controlled SSR-BDC at $P_o = 500$ W, $f_s = 40$ kHz, and $\delta = 10^\circ$: (a) active switch Q_1 , and, (b) active switch Q_5 (25 V/div, 1 A/div, and 400 ns/div).

by 75% as compared to the performance of CF-PSM. The enlarged waveforms of the active switches with VF-PSM are presented in Fig. 22, where ZVZCS turn-on and ZVS turn-off operations can be observed. The voltage and current overlapping areas decrease as compared to CF-PSM.

6.2 Power Control Performances The measured characteristics of output power versus switching frequency are presented in Fig. 23 with respect to the variations of dc voltage ratio G under the condition of VF-PSM closed loop. The PS angle δ is decided in accordance with the setting value of G , then P_o is controlled by changing f_s . Thus, the power controllability of the proposed converter is verified with VF-PSM.

The measured and calculated state-plane trajectories[†] of primary-side and secondary-side LC networks with CF-PSM are drawn in Fig. 24. The voltage and current trajectories

[†] See app. Table 1 in Appendix.

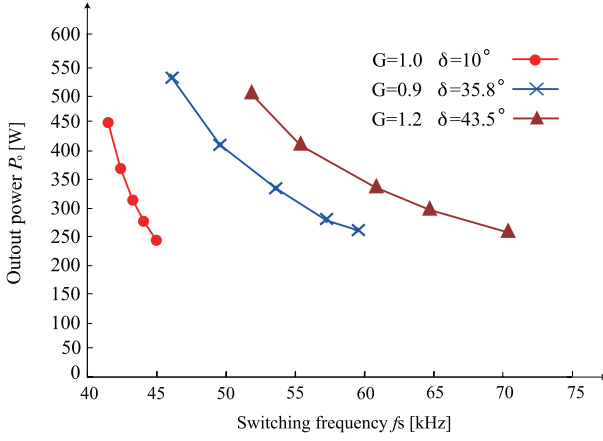


Fig. 23. Measured characteristics of output power versus switching frequency with VF-PSM for the variation of voltage ratio.

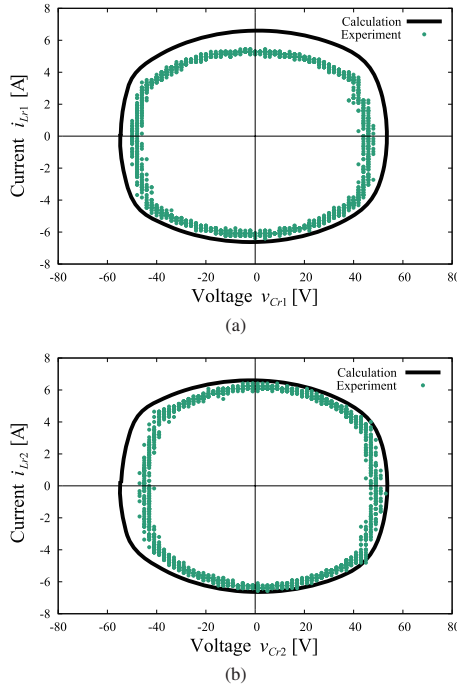


Fig. 24. State-plane trajectories of SSR-BDC with CF-PSM at $P_o = 500$ W, $f_s = 50$ kHz and $\delta = 40^\circ$: (a) primary-side LC network, and (b) secondary-side LC network.

are out of the elliptic orbit due to the switching frequency which deviates from the resonant frequency. The state-plane trajectories of primary-side and secondary-side LC networks with VF-PSM are drawn in Fig. 25. The voltage and current trajectories are the elliptic orbit both in the primary- and secondary-side LC networks controlled by the smaller phase angle. It is clarified from Figs. 24 and 25 that the tank energy diminishes as the switching frequency increases over the resonant frequency, thereby the reactive power increases in the primary- and secondary-side full bridge circuits.

6.3 Power Conversion Efficiency In the beginning of discussion, the measured steady-state characteristics of bidirectional power flows are illustrated in Fig. 26. The output power is actually regulated over the wide range by changing the phase angle δ . The maximum efficiencies are

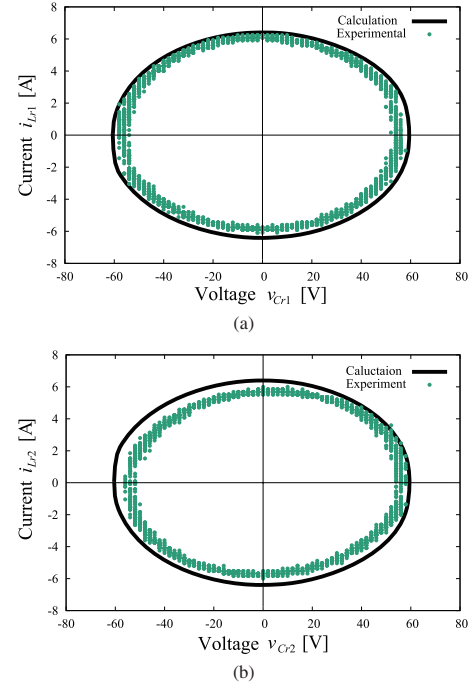


Fig. 25. State-plane trajectories of SSR-BDC with VF-PSM at $P_o = 500$ W, $f_s = 40$ kHz, and $\delta = 10^\circ$: (a) primary-side LC network, and (b) secondary-side LC network.

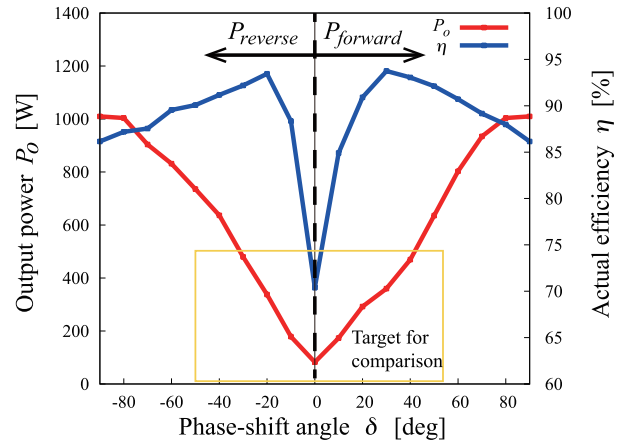


Fig. 26. Efficiency and output power characteristics on the phase angles for the forward- and reverse-mode operations.

observed as 93.7% at $P_o = 360$ W with $\delta = 30^\circ$ in the forward mode ($V_1 \rightarrow V_2$) while 93.5% at $P_o = 340$ W with $\delta = -20^\circ$ in the reverse mode, respectively. The modes of power flow can exchanged continuously in Fig. 26 for the power range of $P_o = 80$ W–1 kW, thus the feasibility of the symmetrical CLLC resonant tank is proven. The efficiency of the low-middle powers is the target to improve by VF-PSM.

The actual efficiencies are compared between the two pulse modulations in Fig. 27. The efficiency of VF-PSM exceeds that of CF-PSM in the power range $P_o = 250$ W–500 W under the conditions of $G = 0.9$, $G = 1$ and partly for $G = 1.2$. The PS angle can be fixed as the optimal value by VF-PSM in accordance with G , whereby the primary and secondary-side circuits can always operate at the best power factors. It should be noted here that the circuit operation suffers from

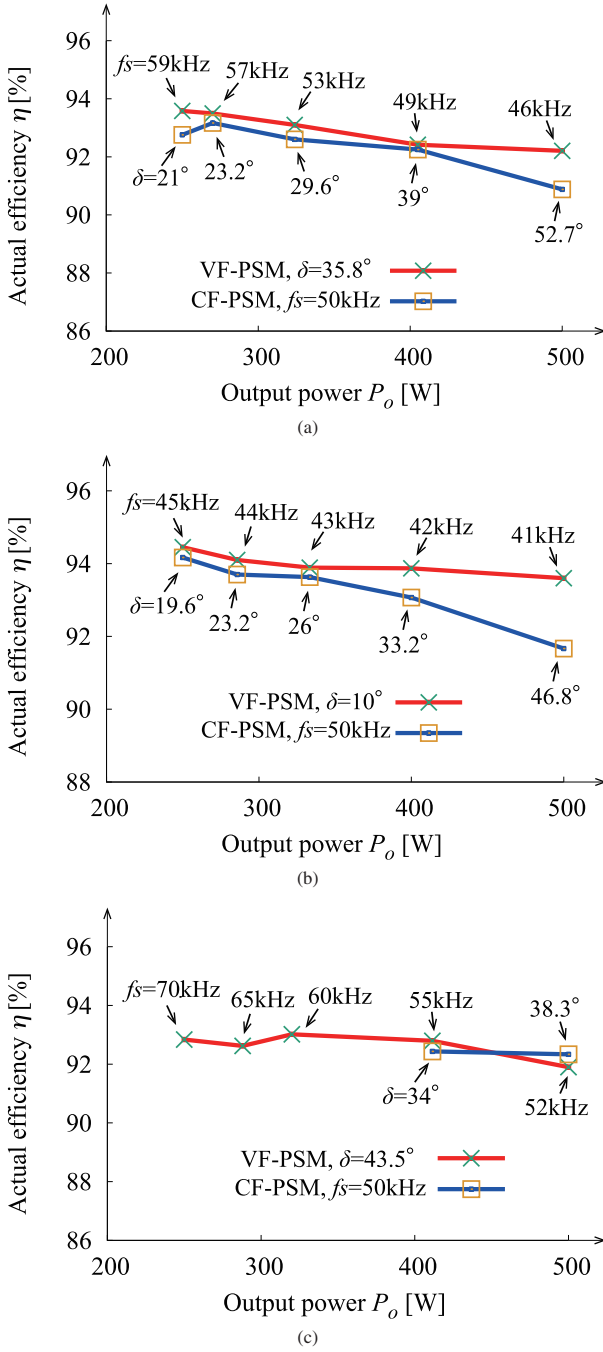


Fig. 27. Actual efficiency curves: (a) $G = 0.9$, (b) $G = 1$, and (c) $G = 1.2$.

the severe hard switching in the light and middle power areas with CF-PSM, therefore the efficiency evaluation is limited from 400 W–500 W in Fig. 27(c). The maximum efficiency is measured as 94.5% at $P_o = 250$ W with $G = 1$ by VF-PSM, and the efficiency improves about 1.4% from 92.3% with CF-PSM to 93.7% with VF-PSM at $P_o = 500$ W. The efficiency with VF-PSM is lower than CF-PSM at $P_o = 500$ W, since the switching frequency of 52 kHz with VF-PSM could cause more turn-off energy loss due to the tail currents of IGBTs than CF-PSM with 50 kHz.

The power loss breakdowns of CF-PSM and VF-PSM prototypes are presented in Fig. 28 with respect to the efficiencies at $P_o = 500$ W and $G = 1$ in Fig. 27(b); $\eta = 91.7\%$

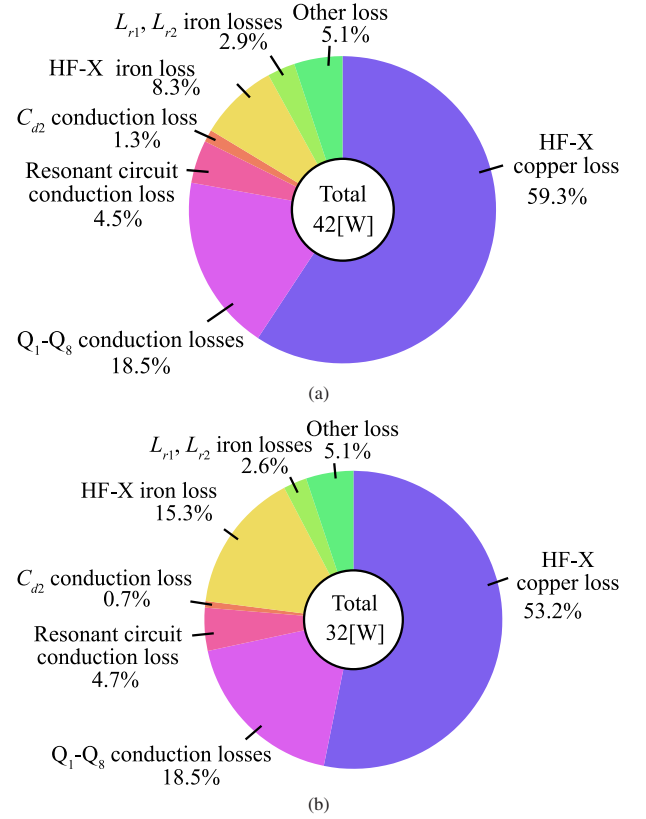


Fig. 28. Power loss analysis of prototype at $P_o = 500$ W and $G = 1$: (a) CF-PSM with $\eta = 91.7\%$ and (b) VF-PSM with $\eta = 93.7\%$.

in CF-PSM and $\eta = 93.7\%$ in VF-PSM, respectively. The RMS currents of the primary- and secondary-side full-bridge circuits are reduced by VF-PSM as mentioned in the subsection 6.1, accordingly the copper loss of the HF-X diminishes as compared to CF-PSM. Moreover, the power losses in the output capacitor filter C_d are reduced by VF-PSM which is more effective for reduction of reactive power. It can be known herewith that reduction of RMS current contributes for efficiency improvement more than that of the switching frequency. The iron loss increases slightly in the loss breakdown with VF-PSM due to the larger time interval in the rectangular two-level bridge-leg voltages v_{ab} and v_{cd} by decreasing the switching frequency.

7. Conclusions

The *CLLC* symmetrical resonant bidirectional dc-dc converter with variable frequency phase shift modulation has been evaluated from the viewpoints of soft switching range and reactive power reduction.

The circuit topology, operation and control strategy have been clarified by the steady-state analysis based on the frequency-domain equivalent circuits and the relevant phasor diagram, whereby the theory and principle of the PS angle determination for minimizing the reactive power with keeping ZVS has been clarified. The practical effectiveness of the resonant bidirectional dc-dc converter has been verified by experiment as compared to the conventional fixed frequency phase shift modulation: Efficiency improves by 1.4% at the rated load and, the peak-peak value of displacement current

reduces by 35% in the output smoothing capacitor, reactive power reduces by 75%, and ZVS operation can be ensured for 10% of the load voltage variation. The advantage of VF-PSM is more outstanding for the multi voltage ratios while CF-PSM is more suitable for the unity voltage ratio in SSR-BDC.

The attractive features of the symmetrical RBDC will be outstanding in the power supplies based on the high frequency-linked dc-dc power conversion with front and rear-end converters. In particular, its multi-phase topology will contribute for achieving high power density of SSTs in the electrified transportation and renewable energy applications.

References

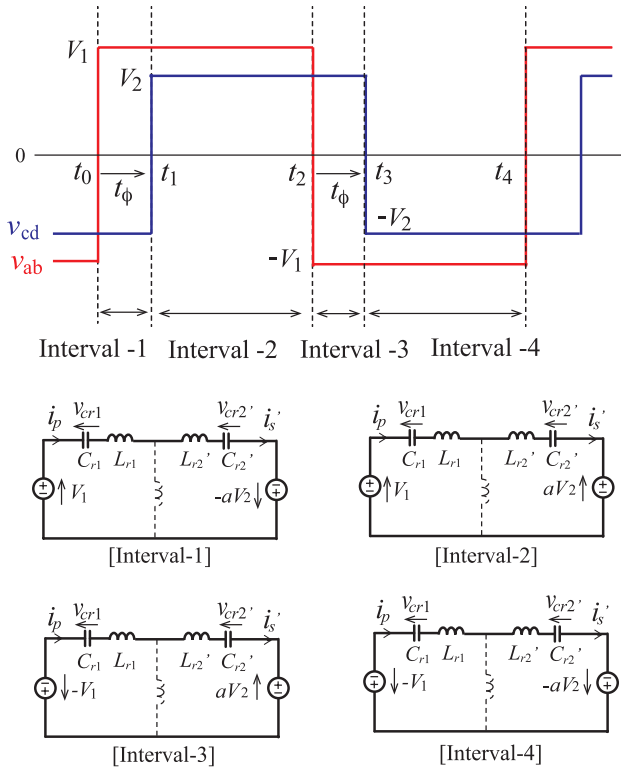
- (1) H. Fan and H. Li: "High-frequency transformer isolated bidirectional dc-dc converter modules with high efficiency over wide load range for 20 kVA solid-state transformer", *IEEE Trans. Power Electron.*, Vol.26, No.12, pp.3599–3608 (2011)
- (2) L. Zheng, R.P. Kandula, K. Kandasamy, and D. Divan: "Single-stage soft-switching solid-state transformer for bidirectional motor drives", in *Proc. 2017 IEEE Energy Conversion Cong. and Expo. (ECCE)*, pp.2498–2505 (2017)
- (3) J.W. Kolar and G. Ortiz: "Solid-State-Transformers: key components of future traction and smart grid systems", in *Proc. 2014 Int. Conf. Power Electron (IPEC)*, pp.22–35 (2017)
- (4) B. Zhao, Q. Song, W. Liu, and Y. Sun: "Overview of dual active bridge isolated bidirectional dc-dc converter for high frequency link power conversion system", *IEEE Trans. Power Electron.*, Vol.29, No.8, pp.4091–4105 (2014)
- (5) W. Chen, P. Rong, and Z. Lu: "Snubberless bidirectional dc-dc converter with new CLLC resonant tank featuring minimized switching loss", *IEEE Trans. Ind. Electron.*, Vol.57, No.9, pp.3075–3086 (2010)
- (6) R. De Doncker, D. Divan, and M.H. Kheraluwala: "A three-phase soft-switched high-power-density dc/dc converter for high-power applications", *IEEE Trans. Ind. Appl.*, Vol.27, No.1, pp.63–73 (1991)
- (7) Y. Shen, X. Sun, W. Li, X. Wu, and B. Wang: "A modified dual active bridge converter with hybrid phase-shift control for wide input voltage range", *IEEE Trans. Power Electron.*, Vol.31, No.10, pp.6884–6900 (2016)
- (8) M. Yaqoob, K.H. Loo, and Y.M. Lai: "Extension of soft-switching region of dual-active-bridge converter by a tunable resonant tank", *IEEE Trans. Power Electron.*, Vol.32, No.12, pp.9093–9104 (2017)
- (9) J. Hiltunen, V. Väisänen, R. Juntunen, and P. Silventoinen: "Variable frequency phase shift modulation of a dual active bridge converter", *IEEE Trans. Power Electron.*, Vol.30, No.12, pp.7138–7148 (2015)
- (10) H. Shi, H. Wen, Y. Hu, and L. Jiang: "Reactive power minimization in bidirectional dc-dc converters using a unified-phasor-based particle swarm optimization", *IEEE Power Electron.*, Vol.99, pp.1–16, DOI 10.1109/TPEL.2018.2811711.
- (11) H. Bai and C. Mi: "Eliminate reactive power and increase system efficiency of isolated bidirectional dual-active-bridge dc-dc converters using novel dual-phase-shift control", *IEEE Trans. Power Electron.*, Vol.23, No.6, pp.2905–2914 (2008)
- (12) A. Taylor, G. Liu, H. Bai, A. Brown, P.M. Johnson, and M. McAmmond: "Multi-phase-shift control for a dual active bridge to secure zero-voltage-switching and enhance light-load performance", *IEEE Power Electron.*, Vol.33, No.6, pp.4584–4588 (2018)
- (13) J. Huang, Y. Wang, Z. Li, and W. Lei: "Unified triple-phase-shift control to minimize current stress and achieve soft-switching of isolated bidirectional dc-dc converter", *IEEE Trans. Ind. Electron.*, Vol.63, No.7, pp.4169–4179 (2016)
- (14) W. Choi, K.-M. Rho, and B.-H. Cho: "Fundamental duty modulation of dual-active-bridge converter for wide-range operation", *IEEE Power Electron.*, Vol.33, No.6, pp.4048–4064 (2018)
- (15) M. Yaqoob, K.H. Loo, and L.M. Lai: "A four-degree-freedom modulation strategy for dual-active-bridge series-resonant converter designed for total loss minimization", *IEEE Trans. Power Electron.*, Vol.34, No.2, pp.1065–1081 (2019)
- (16) G. Buticchi, L. Costa, and M. Liserre: "Improving system efficiency for the more electric aircraft", *IEEE Ind. Electron. Mag.*, Vol.11, No.3, pp.26–36 (2017)
- (17) C. Wang, S. Zhang, Y. Wang, B. Chen, and J. Liu: "A 5-kW isolated high voltage conversion ratio bidirectional CLTC resonant dc-dc converter with wide range gain range and high efficiency", *IEEE Trans. Power Electron.*, Vol.34, No.1, pp.340–355 (2019)
- (18) S. Abe, T. Zaito, J. Yamamoto, and T. Ninomiya: "Operating strategy for bi-directional LLC resonant converter with seamless operation", *Proc. 2014v Int. Power Electron. Conf. (IPEC-Hiroshima)*, pp.1179–1184 (2014)
- (19) M. Yaqoob, K.-H. Loo, and Y. M. Lai: "Fully soft-switched dual-active-bridge series-resonant converter with switched-impedance-based power control", *IEEE Trans. Power Electron.*, Vol.33, No.11, pp.9267–9281 (2018)
- (20) S. Hu, X. Li, and A.K. Bhat: "Operation of a bidirectional series-resonant converter with minimized tan current and wide ZVS range", *IEEE Trans. Power Electron.*, Vol.34, No.1, pp.904–915 (2019)
- (21) T. Jiang, J. Zhang, X. Wu, K. Sheng, and Y. Wang: "A bidirectional LLC resonant converter with automatic forward and back mode transition", *IEEE Trans. Power Electron.*, Vol.30, No.2, pp.757–770 (2015)
- (22) M. Kasper, R.M. Burkart, G. Deboy, and J.W. Kolar: "ZVS of power MOS-FETs revisited", *IEEE Trans. Power Electron.*, Vol.31, No.12, pp.8063–8067 (2016)
- (23) Y. Shen, H. Wang, A. Al-durra, Z. Qin, and F. Blaabjerg: "A bidirectional resonant dc-dc converter suitable for wide voltage gain range", *IEEE Trans. Power Electron.*, Vol.33, No.4, pp.2957–2975 (2018)
- (24) J.H. Jung, H.S. Kim, M.H. Ryu, and J.W. Baek: "Design methodology of bidirectional CLLC resonant converter for high-frequency isolation of dc distribution systems", *IEEE Trans. Power Electron.*, Vol.28, No.4, pp.1741–1755 (2013)
- (25) S. Zou, J. Lu, A. Mallik, and A. Khaligh: "Bi-directional CLLC converter with synchronous rectification for plug-in electric vehicles", *IEEE Trans. Ind. Appl.*, Vol.54, No.2, pp.998–1005 (2018)
- (26) J. Wu, Y. Li, X. Sun, and F. Liu: "A new dual-bridge series resonant dc-dc converter with dual tank", *IEEE Power Electron.*, Vol.33, No.5, pp.3884–3897 (2018)
- (27) S. Zong, G. Fan, and X. Yang: "Double voltage rectification modulation for bidirectional dc/dc resonant converters for wide voltage range operation", *IEEE Power Electron.*, Vol.34, No.7, pp.6510–6521 (2019)
- (28) Y.-W. Cho, W.-J. Cha, J.M. Kwon, and V.-H. Kwon: "High-efficiency bidirectional DAB inverter using a novel hybrid modulation for stand-alone power generating system with low input voltage", *IEEE Trans. Power Electron.*, Vol.31, No.6, pp.4138–4147 (2016)
- (29) X.-F. He, Z. Zhang, Y.-Y. Cai, and Y.-F. Liu: "A variable switching frequency hybrid control for ZVS dual active bridge converters to achieve high efficiency in wide load range", in *Proc. 2014 IEEE Applied Power Electron. Conf. Expo (APEC 2014)*, pp.1095–1099 (2014)
- (30) Q. Tian, A.Q. Huang, H. Bai, J. Lu, H. Teng, M. McAmmond, and A. Brown: "A novel light load performance enhanced variable-switching-frequency and hybrid single-dual-phase-shift control for single-stage dual-active-bridge based ac/dc converter", in *Proc. 42nd Annual Conf. IEEE Ind. Electron. Society (IECON-2016)*, pp.1227–1232 (2016)
- (31) F. Jauch and J. Biela: "Combined phase-shift and frequency modulation of a dual-active-bridge ac-dc converter with PFC", *IEEE Trans. Power Electron.*, Vol.31, No.12, pp.8387–8397 (2016)
- (32) T. Mishima and Y. Koga: "Variable frequency phase-difference controlled CLLC resonant bidirectional dc-dc converter featuring wide-range ZVS performance and reactive power reduction", in *Proc. 2018 IEEE Energy Conversion Cong. and Expo. (ECCE)*, pp.6283–6290 (2018)
- (33) T. Mishima and N. Nakaoka: "Practical evaluation of a ZVS-PWM dc-dc converter with secondary-side phase shifting active rectifier", *IEEE Trans. Power Electron.*, Vol.26, No.12, pp.3896–3907 (2011)
- (34) R.L. Steigerwald: "A comparison of half-bridge resonant converter topologies", *IEEE Trans. Power Electron.*, Vol.3, No.2, pp.174–182 (1988)

Appendix

Fig. 8 is redrawn in app. Fig. 1 for simplicity, where the twelve modes are combined into the four major intervals in accordance with the voltage polarity of v_{ab} and v_{cd} : i) $v_{ab} = V_1 > 0$ and $v_{cd} = V_2 > 0$, ii) $v_{ab} = -V_1 < 0$, and $v_{cd} = V_2 > 0$, iii) $v_{ab} = -V_1 < 0$ and $v_{cd} = -V_2 < 0$, and iv) $v_{ab} = V_1 > 0$ and $v_{cd} = -V_2 < 0$. The state variables of resonant tanks are the resonant capacitor voltage v_{cr1} and HF-X windings current i_p in the primary-side series resonant tank, whereas they correspond to v_{cr2} and i_{cr2} respectively in the secondary side. The equations of the primary- and secondary-side series resonant tanks are summarized in Table 1.

app. Table 1. State Variables Equations in Series Resonant Tanks

Intervals	Primary-side L - C network
$t \in [0, t_1]$	$\frac{(v_{cr1}(t) - \frac{V_1 - aV_2}{A})^2}{(v_{cr1}(0) - \frac{V_1 - aV_2}{A})^2 + (\frac{\zeta}{\sqrt{A}} i_{cr1}(0))^2} + \frac{i_{cr1}^2(t)}{(\frac{\sqrt{A}}{\zeta})^2 \{ (v_{cr1}(0) - \frac{V_1 - aV_2}{A})^2 + (\frac{\zeta}{\sqrt{A}} i_{cr1}(0))^2 \}} = 1$
$t \in [t_1, t_2]$	$\frac{(v_{cr1}(t-t_1) - \frac{V_1 + aV_2}{A})^2}{(v_{cr1}(t_1) - \frac{V_1 + aV_2}{A})^2 + (\frac{\zeta}{\sqrt{A}} i_{cr1}(t_1))^2} + \frac{i_{cr1}^2(t-t_1)}{(\frac{\sqrt{A}}{\zeta})^2 \{ (v_{cr1}(t_1) - \frac{V_1 + aV_2}{A})^2 + (\frac{\zeta}{\sqrt{A}} i_{cr1}(t_1))^2 \}} = 1$
$t \in [t_2, t_3]$	$\frac{(v_{cr1}(t-t_2) + \frac{V_1 - aV_2}{A})^2}{(v_{cr1}(t_2) + \frac{V_1 - aV_2}{A})^2 + (\frac{\zeta}{\sqrt{A}} i_{cr1}(t_2))^2} + \frac{i_{cr1}^2(t-t_2)}{(\frac{\sqrt{A}}{\zeta})^2 \{ (v_{cr1}(t_2) + \frac{V_1 - aV_2}{A})^2 + (\frac{\zeta}{\sqrt{A}} i_{cr1}(t_2))^2 \}} = 1$
$t \in [t_3, t_4]$	$\frac{(v_{cr1}(t-t_3) + \frac{V_1 + aV_2}{A})^2}{(v_{cr1}(t_3) + \frac{V_1 + aV_2}{A})^2 + (\frac{\zeta}{\sqrt{A}} i_{cr1}(t_3))^2} + \frac{i_{cr1}^2(t-t_3)}{(\frac{\sqrt{A}}{\zeta})^2 \{ (v_{cr1}(t_3) + \frac{V_1 + aV_2}{A})^2 + (\frac{\zeta}{\sqrt{A}} i_{cr1}(t_3))^2 \}} = 1$
Remarks	$A = 1 + \frac{C_{r1}}{C_{r2}}, \zeta = \sqrt{\frac{L_{1s}}{C_{r1}}}, L_{1s} = L_{r1} + L'_{r2}$
Intervals	Secondary-side L - C network
$t \in [0, t_1]$	$\frac{(v_{cr2}(t) - \frac{V_1/a - V_2}{B})^2}{(v_{cr2}(0) - \frac{V_1/a - V_2}{B})^2 + (\frac{\kappa}{\sqrt{B}} i_{cr2}(0))^2} + \frac{i_{cr2}^2(t)}{(\frac{\sqrt{B}}{\kappa})^2 \{ (v_{cr2}(0) - \frac{V_1/a - V_2}{B})^2 + (\frac{\kappa}{\sqrt{B}} i_{cr2}(0))^2 \}} = 1$
$t \in [t_1, t_2]$	$\frac{(v_{cr2}(t-t_1) - \frac{V_1/a + V_2}{B})^2}{(v_{cr2}(t_1) - \frac{V_1/a + V_2}{B})^2 + (\frac{\kappa}{\sqrt{B}} i_{cr2}(t_1))^2} + \frac{i_{cr2}^2(t-t_1)}{(\frac{\sqrt{B}}{\kappa})^2 \{ (v_{cr2}(t_1) - \frac{V_1/a + V_2}{B})^2 + (\frac{\kappa}{\sqrt{B}} i_{cr2}(t_1))^2 \}} = 1$
$t \in [t_2, t_3]$	$\frac{(v_{cr2}(t-t_2) + \frac{V_1/a - V_2}{B})^2}{(v_{cr2}(t_2) + \frac{V_1/a - V_2}{B})^2 + (\frac{\kappa}{\sqrt{B}} i_{cr2}(t_2))^2} + \frac{i_{cr2}^2(t-t_2)}{(\frac{\sqrt{B}}{\kappa})^2 \{ (v_{cr2}(t_2) + \frac{V_1/a - V_2}{B})^2 + (\frac{\kappa}{\sqrt{B}} i_{cr2}(t_2))^2 \}} = 1$
$t \in [t_3, t_4]$	$\frac{(v_{cr2}(t-t_3) + \frac{V_1/a + V_2}{B})^2}{(v_{cr2}(t_3) + \frac{V_1/a + V_2}{B})^2 + (\frac{\kappa}{\sqrt{B}} i_{cr2}(t_3))^2} + \frac{i_{cr2}^2(t-t_3)}{(\frac{\sqrt{B}}{\kappa})^2 \{ (v_{cr2}(t_3) + \frac{V_1/a + V_2}{B})^2 + (\frac{\kappa}{\sqrt{B}} i_{cr2}(t_3))^2 \}} = 1$
Remarks	$B = 1 + \frac{C_{r2}}{C_{r1}}, \kappa = \sqrt{\frac{L_{2s}}{C_{r2}}}, L_{2s} = L_{r2} + L'_{r1}$



app. Fig. 1. Primary- and secondary-side bridge-leg voltages with the primary-side referred equivalent circuits.

Tomokazu Mishima (Senior Member) received the B.S., M.S., and



Ph.D. degree all in electrical engineering from The University of Tokushima, Japan in 1999, 2001, and 2004 respectively. Since 2010, he has been with Kobe University, Hyogo, Japan as an associate professor, and engages in the researches and developments of power electronics circuits and systems. His research interests include soft-switching dc-dc converters, resonant converters, and high frequency inverters for industrial, automotive, biomedical, renewable and sustainable energy applications. Dr. Mishima is the recipient of the Best Paper Award in the Eighth IEEE International Conference on Power Electronics and Drive Systems (IEEE-PEDS 2009), Best Paper Presentation Award of the 2012 Annual Conference of the IEEE Industrial Electronics Society (IECON), and IEEE Transactions on Power Electronics 2017 Outstanding Reviewer Award. He serves as an associate editor of IEEE Transactions on Power Electronics and a secretary of IEEJ (The Institute of Electrical Engineering of Japan) Transactions on Industry Applications. Dr. Mishima is a member of IEICE (The Institute of Electronics, Information and Communication Engineers), and JIPE (The Japan Institute of Power Electronics), and a senior member of IEEE.

Yasutaka Koga (Non-member) graduated from Osaka Prefecture



University of College in 2015. He received the B.S. and M.S. degrees in the maritime sciences from Kobe University, Japan in 2017 and 2019, respectively. His main research interests include the resonant converter applications for renewable and sustainable energy generation systems. He currently engages in developments of medical equipments in DAIKIN Industries, Ltd. in Osaka, Japan. Mr. Koga was a student member of IEEJ from 2017 to 2019.